Department of Mechanical and Aerospace Engineering

Honours Thesis

Transient Supersonic Jets

Author
Brodie James Norfolk

Supervisor
Daniel Edgington-Mitchell

Laboratory for Turbulence Research in Aerospace and Combustion

Abstract

This thesis aims to explore the fundamental fluid dynamics for transient supersonic jets by means of varying the exit flow nozzle geometry and introducing an impingement plate set at 90° to the oncoming flow. The study of transient supersonic jets has applications in pressure gain combustion (PGC). PGC is a constant volume combustion process applicable to gas turbines that operates by increasing the stagnation pressure entering the turbine via heat released from combustion. Increasing the turbine inlet pressure allows for considerably more work to be extracted when the turbine expands the flow back to the free stream pressure. The unique design presented in PGC engines predicts possible advances in thermodynamic efficiencies leading to significantly lower fossil fuel consumption. The experiment undertaken compares flow regimes of NUMBER and NUMBER Mach numbers for each nozzle geometry at impingement plate positions of 1 and 4 inner nozzle diameters. Transient jet impingement has previously been studied, although it is absent of extensive, repeated experiments, high quality schlieren, and variable exit geometry. This thesis aims to address absences in the literature and explore in detail the shock-vortex interaction during jet impingement. The fundamental fluid dynamics under investigation are; nozzle geometry effects on the shock-vortex interaction and jet impingement, and Mach number variations on all of the latter.

Acknowledgements

The author would like to thank those who provided advice and guidance throughout this project. Particularly Dr. Daniel Edgington-Mitchell who supervised the year long project and gave integral feedback, and Bhavraj Thethy for working tirelessly to prepare a functioning laboratory and contributing useful discussions. The author also wishes to acknowledge fellow undergraduate and graduate students including Thomas Knast, Sam Lock, Anesu Junior Kusangaya, and Marcus Wong for assisting in laboratory development and providing key suggestions. The efforts of the Mechanical Engineering Workshop at Monash University are also appreciated for their work in the manufacturing of facility components. Finally, the author thanks his family and friends for their unwavering support throughout all 5 years of his double degree.

Contents

List of Tables

List of Figures

Nomenclature

M_1	Ambient Mach number
P_1	Ambient pressure, Pa
P_4	Shock tube driver section pressure, Pa
T_p	LED pulse width timing, seconds
U_i	Incident shock wave air velocity, m/s
U_1	Ambient air velocity, m/s
U_4	Shock tube driver section air velocity, m/s
X_{image}	Image length, mm
γ_1	Ambient specific heat ratio
γ_4	Driver specific heat ratio

1 Introduction

1.1 Motivation

Understanding transient supersonic jets is integral for the integration of pressure gain combustion in ground and aerospace gas turbine applications. PGC offers a significant gain in thermodynamic efficiencies and subsequent reduction in fossil fuel consumption. The literature adeptly describes the fluid dynamics for a transient supersonic jet propagating from a no nozzle shock tube, and the impingement of a transient supersonic on plates set to varying angles in respect to the flow. However, there is an absence of extensive, repeated experiments, high quality schlieren, and variable exit geometry. This thesis is motivated by absences in the literature and aims to explore in detail, the shock-vortex interaction during jet impingement.

1.2 Aims

This thesis aims to explore the fundamental fluid dynamics for transient supersonic jets by means of varying the exit flow nozzle geometry and introducing an impingement plate set at 90° to the oncoming flow. The propagation and time dependent growth of transient and trailing jet Mach disks will be investigated in an attempt to address absences in the literature, and explore in detail the shock-vortex interaction during jet impingement. The pixel relative velocity of the impinging shock wave for plate and no plate experiments will be extracted from the data in order to define each individual flow regime. The fundamental fluid dynamics under investigation are; nozzle geometry effects on the shock-vortex interaction and jet impingement, and Mach number variations on all of the latter.

2 Background Theory

2.1 Pressure Gain Combustion

Gas turbine engines are an integral component for the function of ground based power generation and aircraft engines. They account for a large percentage of power generation world wide. Thermodynamic cycle advances in gas turbine design play an important role in preventing the growth of emissions pollution and prolonged global warming [10]. Pressure gain combustion (PGC) shown in Figure 1 is one possible to method of efficiency improvement. PGC is a constant volume combustion process that operates by increasing the stagnation pressure entering the turbine via heat released from combustion. Increasing the turbine inlet pressure allows for considerably more work to be extracted when the turbine expands the flow back to the free stream pressure. PGC optimises gas turbine thermodynamic cycle efficiency, and has the potential to increase current engine efficiency up to 10% [11].

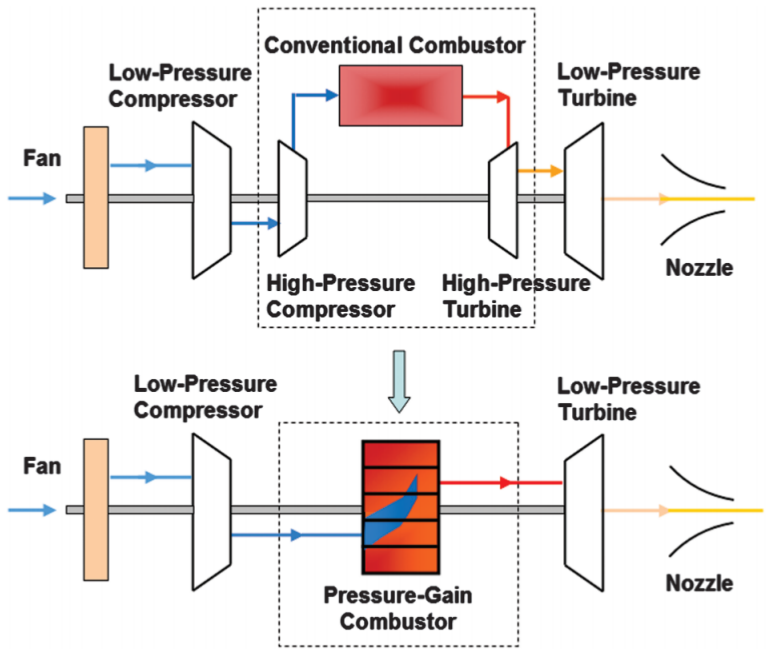

Figure 1: PCG design concept [2].

PGC is at peak efficiency when accomplished through detonation driven combustion, this involves the implementation of detonation waves within the combuster to cause an increase in the temperature and pressure of the fuel-air mixture [12]. During combustion, detonation waves produce flow at supersonic velocities leading to an approximate constant volume and significant pressure gain across the combustor. For supersonic velocities high pressure turbine inlet flow must be steady. A possible method to achieve steady flow at the turbine inlet is via the implementation of a pulse detonation engine [13] with an equalising plenum chamber. Wear on the first stage of the turbine presents itself as one of the most significant problems of PGC implemetation in current engines. Replacing the combustor in a conventional gas turbine with a pulse detonation combustor (PDC) will result in the propergating detonation waves to converge on the first stage of the turbine. This overtime can lead to concentrated wear on the first stage of the turbine high wear stress points [14]. To alleviate turbine wear, the utilization of a high pressure plenum chamber is placed at the exit of the PDC, and creates steady flow conditions effectively shielding the first stage of the turbine from combustion detonations. It remains unclear on how to integrate a pressure plenum into a PDC design.

2.2 Transient Supersonic Jet

The fluid dynamics characterising the governing flow at the exit of PDC is defined as a shock-driven, transient, supersonic jet process [15]. The governing flow can be classified into several different stages [16]. The first stage of jet evolution is defined by the diffraction of a shock wave around the corners of the tube exit as shown in Figure 2. This region is bounded by the curved part of the incident shock, the nozzle lip, and a reflected sound wave. In the next

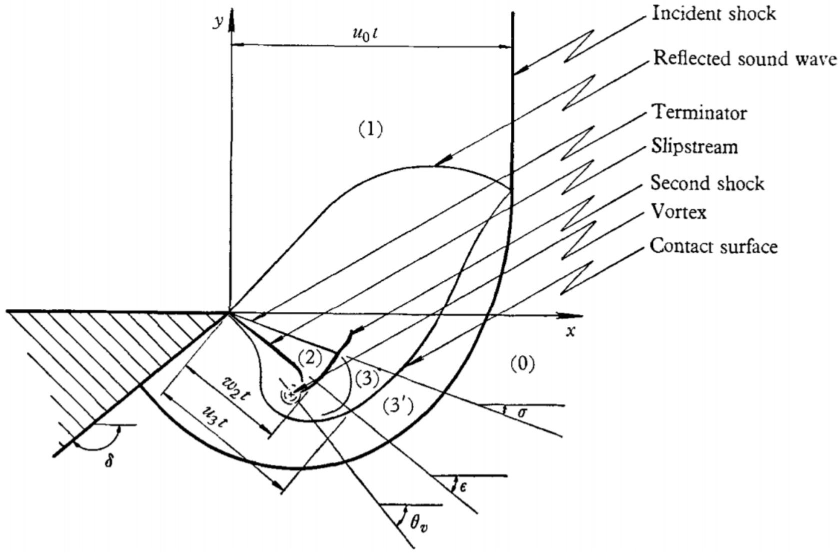

Figure 2: Features of the diffraction pattern [3]

stage of jet evolution, a vortex ring is generated by the roll-up of the shear layer due to Kelvin-Helmholtz type instabilities along the slipstream at the nozzle lip [17, 18]. Kelvin-Helmholtz instabilities exist within the shock as a result of external perturbations (inhomogeneities in the flow) producing oscillations in the vortex sheet separating fluids with different flow characteristics. This structure propagates down the jet axis, and is simultaneously accompanied by the translation of a curved barrel shock formed initially at the nozzle lip. This instigates the formation of a curved Mach disk for a ratio of the nozzle exit to free-stream pressure exceeding 2.06 [19]. MORE ON MACH DISK

A triple point occurs between the leading edge of the barrel shock, the second shock, and the Mach disk. Given a sufficiently strong jet, a slip surface is generated downstream of the triple point. The first shock cell is formed in the third stage of jet evolution which is marked by the pinch-off phenomenon of the vortex ring, and signals the start of the trailing jet phase [20]. Separation of the vortex ring from the flow structure is driven by Kelvin-Helmholtz instabilities within the shear layer of the trailing jet [21]. The final stage of the supersonic jet is defined by the point at which the transient jet and vortex are no longer joined and the trailing jet forms. This is accompanied by the formation of a quasi-steady shock cell in self-sustained oscillation, radiating strong pressure waves. These four stages of jet evolution are illustrated in Figure 3.

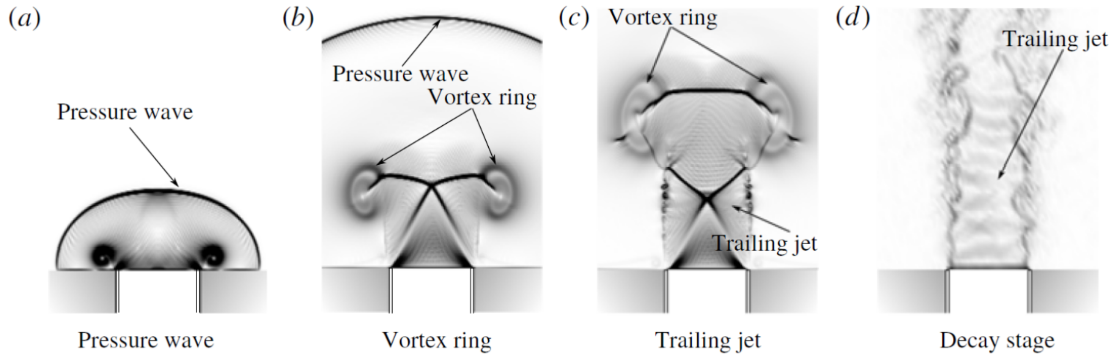

Figure 3: Evolution of the transient supersonic jet. (a) Diffracting shock/Pressure wave. (b) Axial translation of the vortex rings, formation of the curved shock and an unsteady Mach disk. (c) Formation of the trailing supersonic jet. (d) Decay of the trailing jet and the end of the transient jet process. [4]

2.3 Transient Jet Impingement

Investigation into the high pressure plenum chamber required for PDEs currently has not been undertaken within the field. However, the flow dynamics is considered analogous to the impingement of a transient supersonic jet on a flat plate. The governing dynamics of transient jet impingment can be classified into serveral stages. The physical process is initially characterised by the reflection of the incident shock wave on the impinging plate. The reflected shock wave propargates back towards the nozzle and interacts with the approaching vortex ring. The central section of the reflected shock wave is captured by the embedded rearward-facing shock at the centre of the vortex ring, and is intensified by the opposing high-speed flow. Simultaneously, the outer section of the shock wave is diffracted by the vortex core. This process results in the formation of a toroidal shock wave which focuses in the trailing jet along the longitudinal axis of flow. The next stage of the fluid dynamics is defined by the impingement of the propagating vortex ring. Initially, as the vortex ring approaches the wall, its propagation velocity decreases and its diameter increases due to the adverse pressure gradient present [5]. After votex impingement the vortical flow undergoes rapid radial expansion developing a boundary layer on the surface, which slows down the flow and increases the pressure distribution over the plate. After a given duration that is dependent on the initial incident Mach number, the boundary layer separates from the plate and the flow rolls up generating a series of secondary vortices. This also occurs at the thin shear layer present between the jet flow and the exterior fluid as the region rolls up due to Kelvin-Helmholtz instabilities. This produces small interacting secondary vortex rings that propagate towards the plate [22]. Cumulative interactions between the primary and secondary wall vortex rings result in a near standing lift off of the pair. The secondary ring subsequently merges with the primary ring, and the weakened newly formed vortex ring continues to translate down the plate. Stages of impingement are illustrated in Figure 4 below.

For a plate of variable angle, the lower core of the vortex ring impinges initially and generates an asymmetric set of secondary vortices. These new flow structures orbit around the

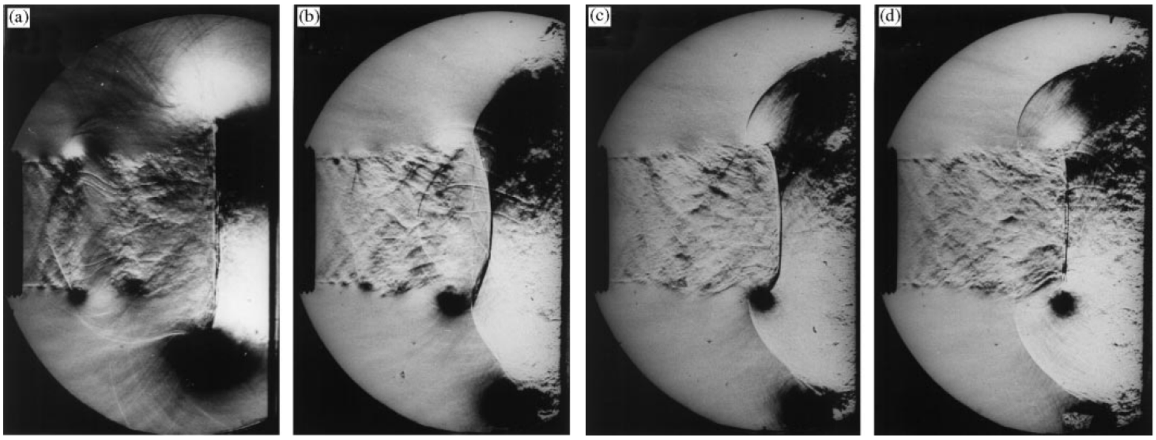

Figure 4: Evolution of jet impingement. (a) Impingement of vortex ring. (b) Vortex ring translates down the plate. (c) Secondary vortex formation. (d) Lift-off of votex rings and dissapation. [5]

main vortex, creating a temporarily thicker boundary layer at the lower end of the flow field. Again after a period of time, dependent on the incident Mach number, he boundary layer separates from the plate. This results in the vortex ring pivoting on the lower core, undergoing negligible deformation, and propergates towards the surface plate. The upper core then impinges on the plate and the upper wall vortex is generated. This new structure begins to expand radially increasing in thickness due to the remaining jet flow. While simultaneously, the lower wall vortex propagates around the outer limits of the main vortex, stops expanding, and dissipates into a thin structure. The impinging jet continues to feed into the upper section of the flow field generating wall vortices with a thicker upper core. For lower angles of plate alignment, the flow field shows an increase in overall velocity and visible curvature of the vortex ring structure during impingement. The toroidal shock wave that forms as a result of impingement propagates perpendicularly with respect to the surface [23].

2.4 Acoustic Noise

The far-field noise developed by the shock wave-vortex interaction can be decomposed into three components, the sound field due to the formation and evolution of the vortex ring, the reflection shock and vortex ring interaction noise production, and the noise due to impingement of the ring on the plate. The plate-votex ring impingement noise is produced by fluctuating pressure due to the deformation and stretching of the vortex ring, formation and growth of a secondary wall vortex ring, and lifting-off of the primary-secondary vortex ring pair [24].

3 Experimental Methods & Analysis Techniques

3.1 Technical University of Berlin Pulse Detonation Combustion Facility

The initial imaging processing work conducted in this thesis was tested on experimental data supplied by the Technical University of Berlin's (TBU) pulse detonation combustion (PDC) facility. The PDC facility at TBU consists of a 685mm long deflagration-to-detonation transition (DDT) section with a tube diameter of 40mm, and 825 mm exhaust section with a tube diameter of 30mm. The DDT supply gas is a combination of hydrogen and air. DDT is initiated with a number of orifice plates, and the leading detonation wave is tracked using a number of ionisation and pressure sensors placed throughout the exhaust tube. The governing flow dynamics were captured using schlieren measurements positioned in a Toepler Z-Type schlieren system [7]. The schlieren system is constructed using two 8in parabolic mirrors with a high speed LED providing the necessary light source [25]. The images were captured using a Photron SA-Z camera for converging and diverging nozzles. The experimental layout is shown in Figure 5.

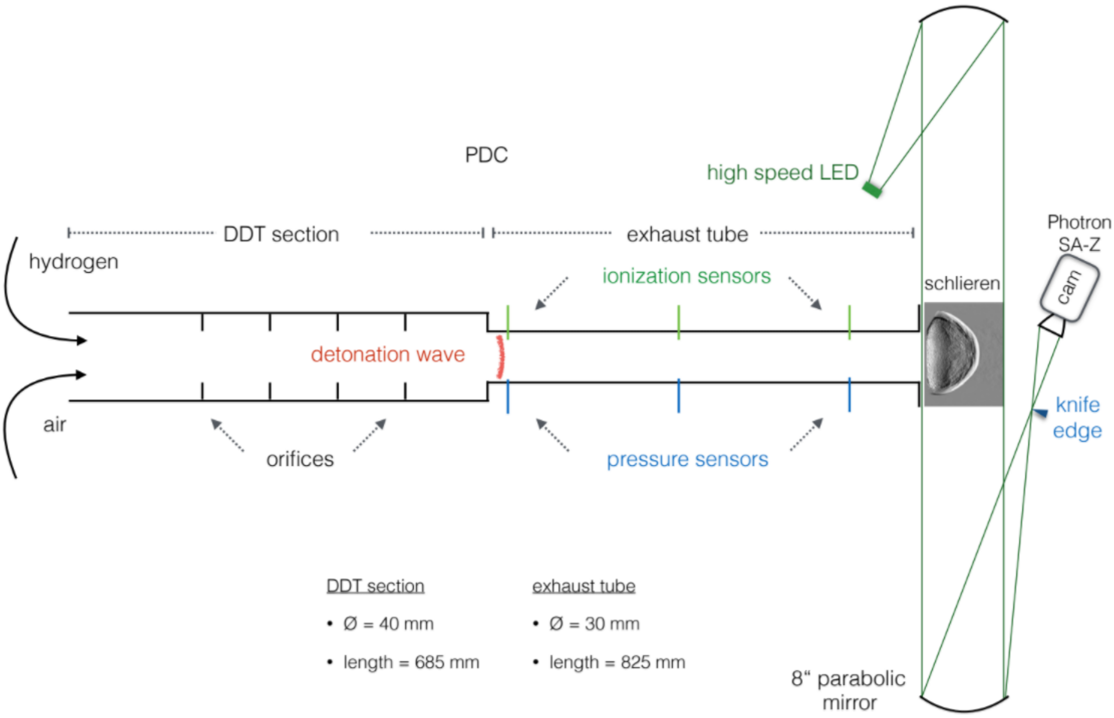

Figure 5: Shock tube facility schematic at TUB. Major parts of the system have been labelled [6].

3.2 Shock Tube Facility

The experiments presented were conducted in the LTRAC Supersonic Jet Facility. A schematic of the facility is shown in Figure 6.

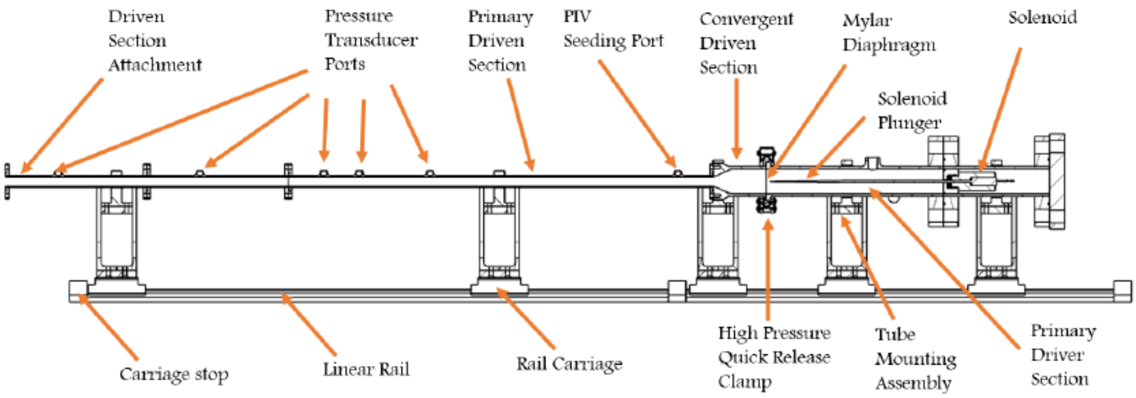

Figure 6: Shock tube facility schematic. Major parts of the system have been labelled.

The facility utilises compressed air delivered by the Monash University compressed air supply system. To produce a canonical transient supersonic jet a shock tube model is adopted [26]. A typical shock tube consists of a high pressure section (driver section) and a low pressure section (driven section) separated by a diaphragm. Air enters the driver section until a desired pressure is reached, the diaphragm is then ruptured via a puncture from an actuated pin. Following the rupture, compression waves are fired down the driven section by the high pressure gas in the driver. As these compression waves travel down the tube they coalesce and form a shock wave that propagates into the test section, diffracts, and produces a transient supersonic jet.

For the aims of this thesis, the supersonic transient jet will be studied with varied nozzle designs including a convergent, divergent and convergent-divergent configuration. Transient flow impingement will be tested via a flat plate set at 90° to the flow. This impinging plate is set exactly at an angle of 90° to the flow by a sequence of precisely 90° connecting supports to the shock tube. The three nozzle designs and impingement plate will be integrated into the existing LTRAC Supersonic Jet Facility.

The relationship between the driver (4) pressure ratio and the ambient (1) pressure of the system is shown in Equation 1, and was utilised to calculate the design incident Mach number propagating from the shock tube [27]. Figure 7 illustrates the effect of specific heat capacity ratio on the relation between incident Mach number and pressure ratio. Helium gas has increasingly lower pressure ratios for higher Mach numbers in comparison to air, and as a result was chosen as the driver section supply gas.

$$\frac{P_4}{P_1} = \frac{2\gamma_1 M_1^2 - (\gamma_1 - 1)}{\gamma_1 + 1}\left(1 - \frac{\gamma_{4-1}}{\gamma_{1+1}}\frac{U_1}{U_4}\left(M_1 - \frac{1}{M_1}\right)\right)^{-2\gamma_4/\gamma_{4-1}} \tag{1}$$

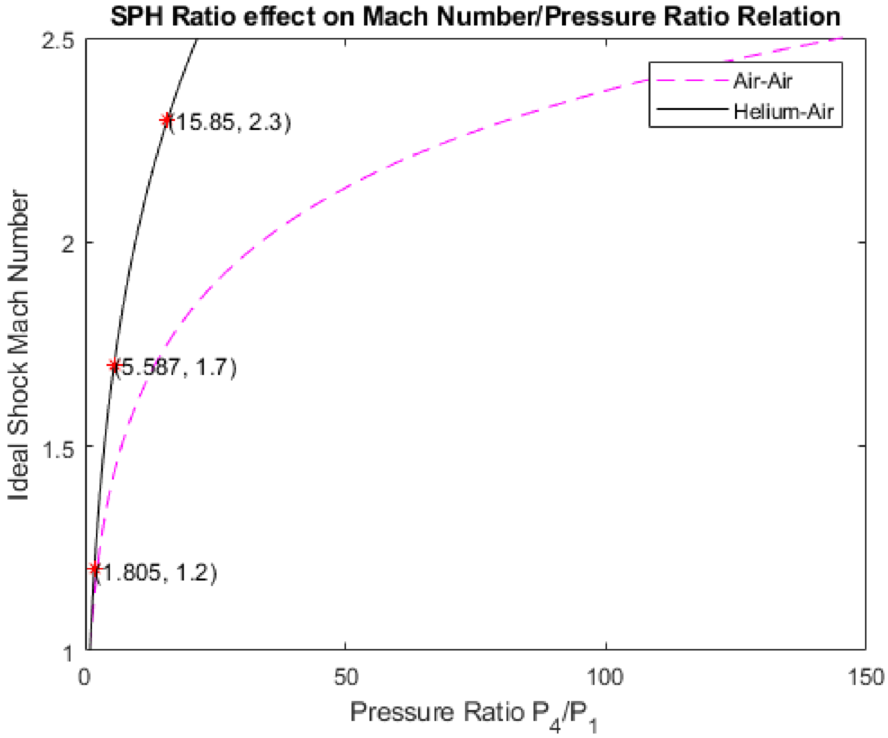

Figure 7: Specific Heat Capacity Ratio effect on Mach Number/Pressure Ratio Relation.

3.3 Schlieren Imaging

Schlieren imaging is a visualization technique that utilises the refraction of light to produce focused optical images of transparent media. Point source light is collimated and passed through a test region containing a transparent media with inhomogeneities. Light entering the test region will refract at varied degrees according to an inhomogeneous density distribution present. When refraction occurs the curvature ϵ of light, for a given test section length L, and refractive index n_0 can be calculated using Equations 2 and 3 for x and y orthogonal coordinates. The light is then refocused and a knife-edge is used to partially block a fraction of incident light from the screen or camera.

$$\epsilon_x = \frac{L}{n_0}\frac{\delta n}{\delta x} \tag{2}$$

$$\epsilon_y = \frac{L}{n_0}\frac{\delta n}{\delta y} \tag{3}$$

The shock-driven, transient, supersonic jet is measured using a Toepler Z-type schlieren apparatus [7] (illustrated in Figure 8). This Z-type apparatus incorporates parabolic mirrors to collimate the light. Parabolic mirrors eliminates problems associated with chromatic aberration and provides a unique advantage for imaging in comparison to systems using lenses. However, the use of mirrors introduces common imaging problems including coma and astigmatism. Coma is the result of off-axis, incorrect parabolic mirror tilting and disrupts the collimated light beam. It also causes the focal point of the parabolic mirrors to spread into a line. This issue is resolved by careful calibration of each parabolic mirror titling to achieve an overall cancelling effect. Astigmatism is similarly caused by tilting the parabolic mirror off-axis. It occurs due alternating path lengths of light dependent on their respective optical plane. Astigmatism results in different focal points for each plane of propagating light and requires the knife-edge to be positioned for different density gradients. For Z-type schlieren configurations, coma and astigmatism is minimised by restricting the offset angle (tilt) of the parabolic mirrors to minimum achievable values. Careful calibration prior to experimentation is required to avoid problems associated with coma and astigmatism. This involves correcting mirror allingments, adjusting the knife edge, and positioning the camera distance until the desired image is displayed. The parabolic mirrors used in the facility have an an effective focal length of 1200mm and the light source was supplied by a pulsed LED [25].

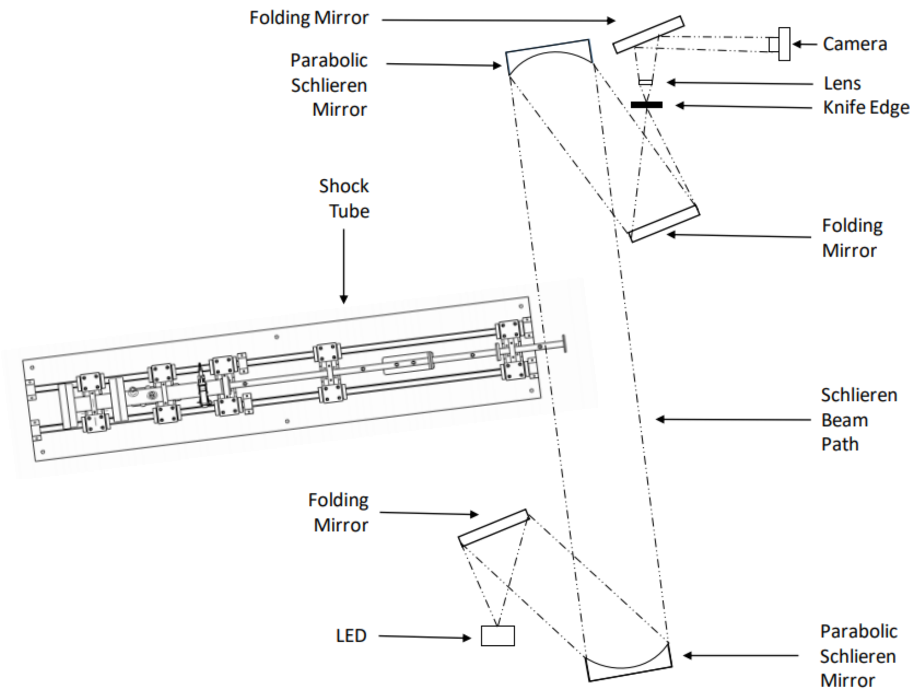

Figure 8: Detailed schlieren system diagram.

3.3.1 High Resolution Imaging

High spatial-resolution images were captured using the Chronos camera with a resolution of 1280x1024 pixels at 1057 frames per second (fps). Image sets varied in size and were determined by the fluid dynamic structures captured. If a set contained significant detail of the transient process by nature it was larger. Smaller sets were recorded if the respective trailing jet displayed unique flow qualities. Image sets containing information on the transient process were of more significance given the aims of this thesis and were a priority for capturing, this led to the implementation of high speed cameras. The schlieren parameters for several conditions using the Chronos camera are included in Table 1, Figure 9 shows the physical representation of each parameter.

3.3.2 High Speed Imaging

High speed images were captured using the Shimadzu HPV-1 camera with a resolution of 312 x 260 pixels and a frame rate of up to 1 million fps. Image sets were approximately constant give this camera was utilised to specifically capture the transient supersonic jet. Image quality provided by the Shimadzu HPV-1 is low in comparison to the Chronos camera. As a result, data from the Shimadzu was solely used for flow analysis and not flow feature discussions. The schlieren parameters for several conditions using the Shimadzu HPV-1 camera are included in Table 2, Figure 9 shows the physical representation of each parameter.

Table 1: High spatial-resolution schlieren parameters.

b (mm)	h (mm)	Magnitude	f_3 (mm)	e (mm)
50	20	0.169	204.911	201.448
35	15	0.241	294.902	287.782
20	10	0.422	525.836	503.620
12	6	0.704	902.949	839.366

Table 2: High speed schlieren parameters.

b (mm)	h (mm)	Magnitude	f_3 (mm)	e (mm)
50	20	0.721	926.821	859.956
35	15	1.031	1369.672	1228.509
20	10	1.803	2622.970	2149.891
12	6	3.006	5123.180	3583.152

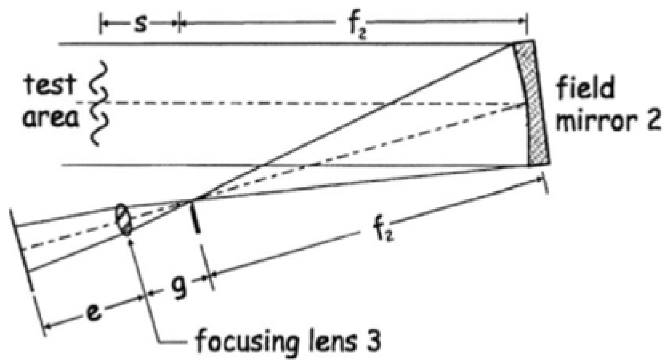

Figure 9: Schlieren parameters [7].

3.3.3 Limitations

Schlieren imaging has a number of limitations. Firstly, schlieren images are constructed using density gradients within the test region. The gradients are integrated over the optical path and as a result, images are developed as two-dimensional projections of an original three-dimensional fluid flow. This introduces possible incorrect projects of three-dimensional features. Additionally, the technique is line-of-sight dependent as the light must be collimated and refocused in order to produce an image. This restricts the layout of test section and sets requirements on the amount of space required for the apparatus.

3.4 Facility Development and Calibration

3.4.1 Nozzle Design

A convergent, divergent, and convergent-divergent nozzle was designed using CAD and manufactured by the Engineering department Mechanical Workshop. All three nozzle designs adopt geometry ratios implemented in the nozzles designed by Technical University of Berlin (TUB). To prevent reflecting flow and acoustic feedback loop interference, each nozzle geometry was designed with a 60° exterior angle and a $0.5mm$ lip [28]. Each nozzle design and subsequently manufactured component is shown in Figures 10, 11, and 12 below.

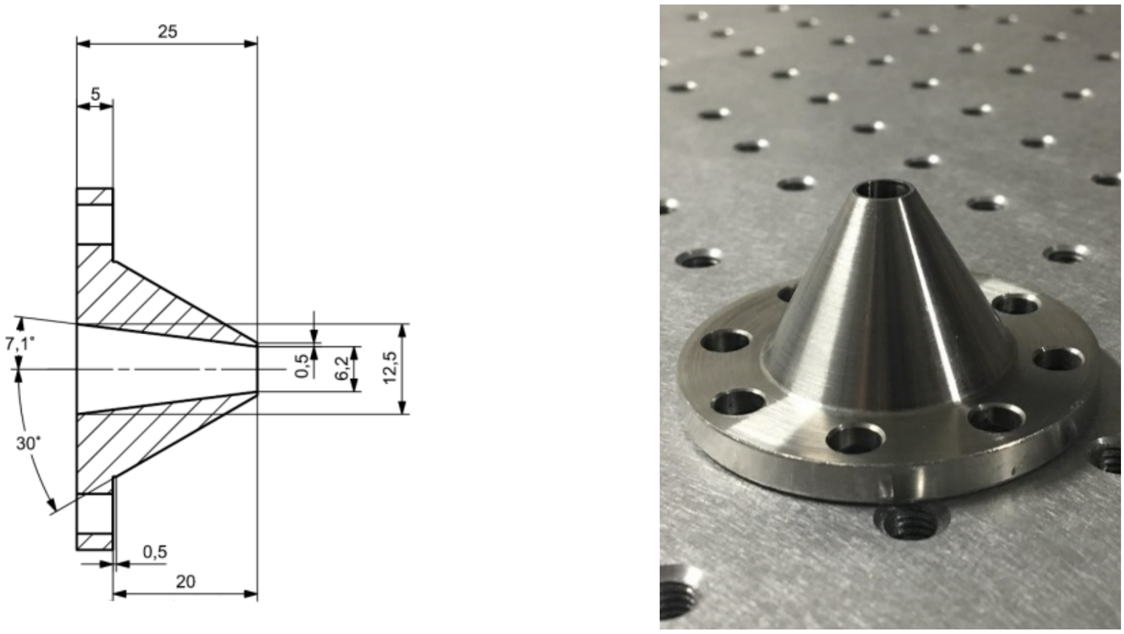

(a) CAD design (all measurements are in mm).

(b) Manufactured nozzle.

Figure 10: Convergent nozzle.

3.4.2 Impingement Plate Design

The impingement plate as shown in Figure 13 is constructed such that it is 90° to the direction of the flow, and will appear infinite in the reference frame of the oncoming flow. The plate is mounted on rails which fix to the shock tube rig, this construction can be adjusted to 1 and 4 inner diameters. This construction allows the plate to be removed and replaced with another plate of alternate geometry for future research. During the evolution of a transient supersonic jet, the vortex is fully formed at approximately 3 inner diameters from the exit for a conventional, no nozzle, shock tube [23]. As a result, an impingement plate distance is chosen below and above this limit at 1 and 4 inner diameters, respectively.

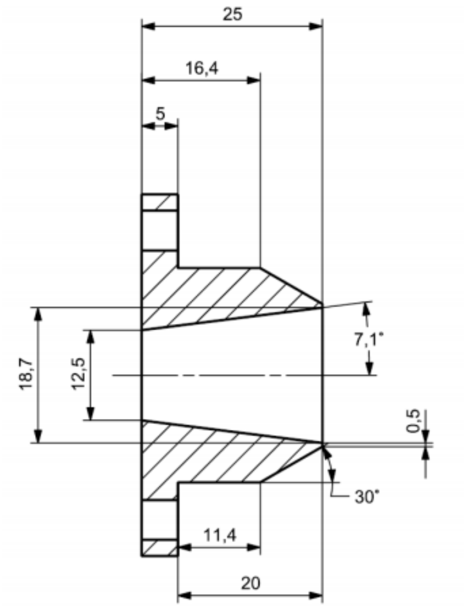

(a) CAD design (all measurements are in mm).

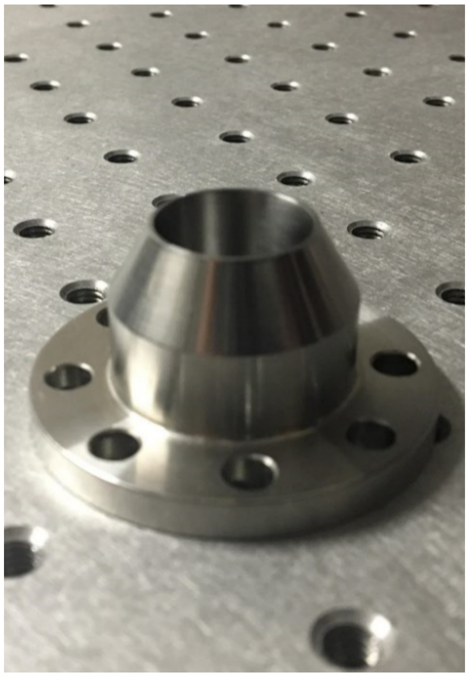

(b) Manufactured nozzle.

Figure 11: Divergent nozzle.

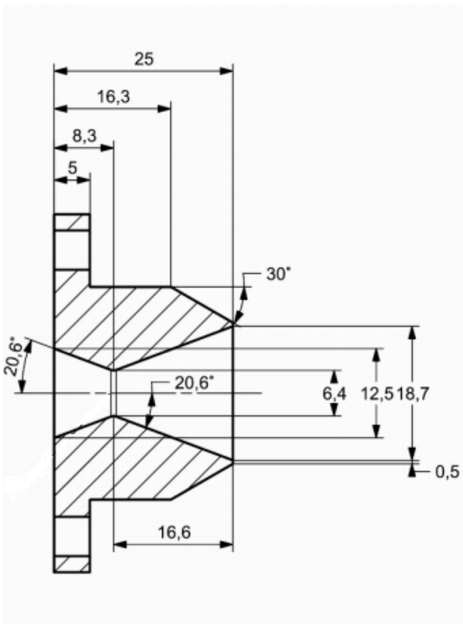

(a) CAD design (all measurements are in mm).

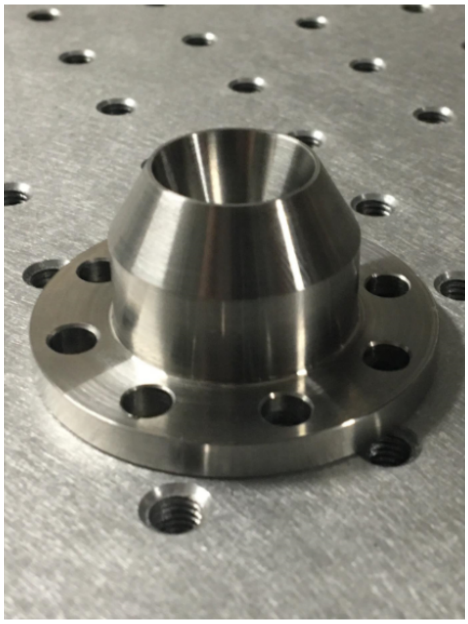

(b) Manufactured nozzle.

Figure 12: Convergent-divergent nozzle.

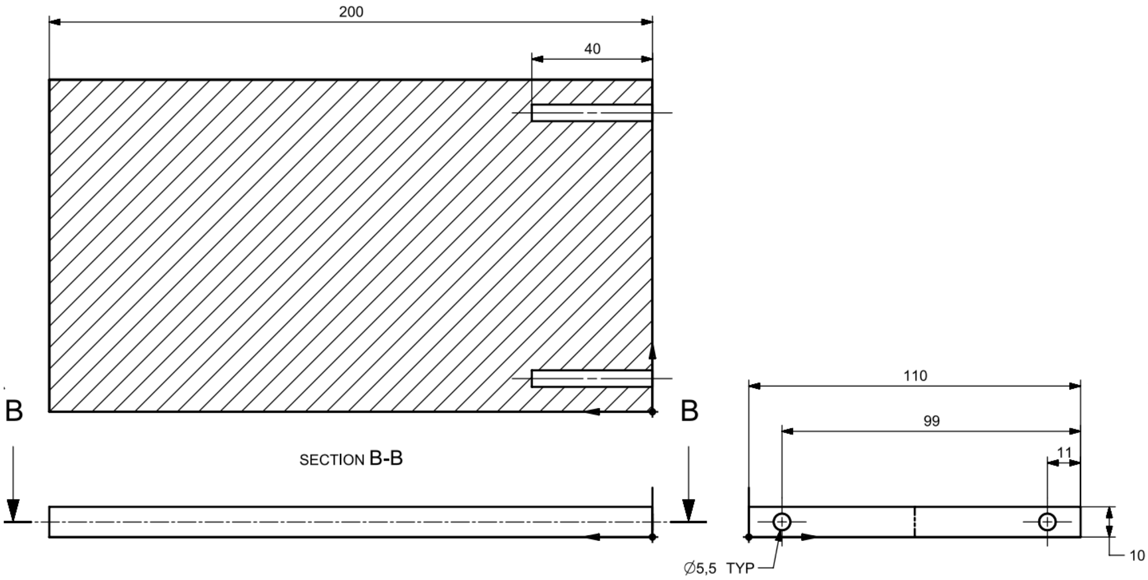

Figure 13: Impingement plate CAD design (all measurements are in mm).

3.4.3 Impingement Plate Development

The first iterative design of the plate resulted in a significant unexpected wobble during jet impingement. Figures 15, 16, and 17 are constructed using post processing techniques detailed in Section 4, and illustrates the pixel displacement of the plate resulting from flow impingement for design iterations 1, 2, and 3 respectively. Figure 15 illustrates the first design iteration which involved the incorrect tightening of impingement plate bolt fixings. This caused an oscillatory pixel displacement response as a result of the significant freedom of movement given to the plate by inadequate fastening. The pixel displacement decreases as a function of increasing frame number, this is governed by the initial transient supersonic jet impingement, under-expanded trailing jet impingement, and the decreasing back pressure of the shock tube. Figures 16 and 17 represent the pixel displacement for an adequately fastened impinging plate and a reinforced impinging plate structure. Both figures highlight the evolution of the transient supersonic jet. Initially at frame 0 the pixel displacement is similarly 0 given impingement has not yet occurred. The sudden jump in pixel displacement in frame 1, and subsequent pixel displacement in the following frames represents the impingement of the evolving transient supersonic jet. As the supersonic jet becomes an under-expanded trailing jet the relative pressure of the flow on the plate decreases as the back pressure in the shock tube decreases. Given the limitations of the recording time for the Chronos camera, the full evolution of the under-expanded trailing jet was not captured and as a result, the pixel displacement shown in Figure's 15, 16, and 17 have final values not representative of pixel displacement at the end of the under-expanded jet process, and once the back pressure in the shock tube is approximately equal to atmospheric pressure. If the full fluid dynamics process was captured it is to be expected that the pixel displacement once the back pressure within the shock tube reaches atmospheric pressure, or once the pressure induced on impinging plate is negligible would be 0. This design error was addressed between iterations 2 and 3 (Figures 16 and 17) with the addition of support brackets as shown in Figure 14. The position of the support brackets was chosen such that interference with the transient supersonic jet and impingement by-products was not possible. This design change had little affect on the pixel displacement of the impingement plate. In comparison to Figure 16, Figure 17 contains a lower magnitude minima pixel displacement value although, the range between maxima and minima stays approximately the same for both iterations. This suggests the design of the impinging plate needs further modification with additional supports and improved fastening bolts. However, in Figures 16 and 17 the largest pixel displacement approximates to 0.6% and for the purposes of this thesis will be considered negligible.

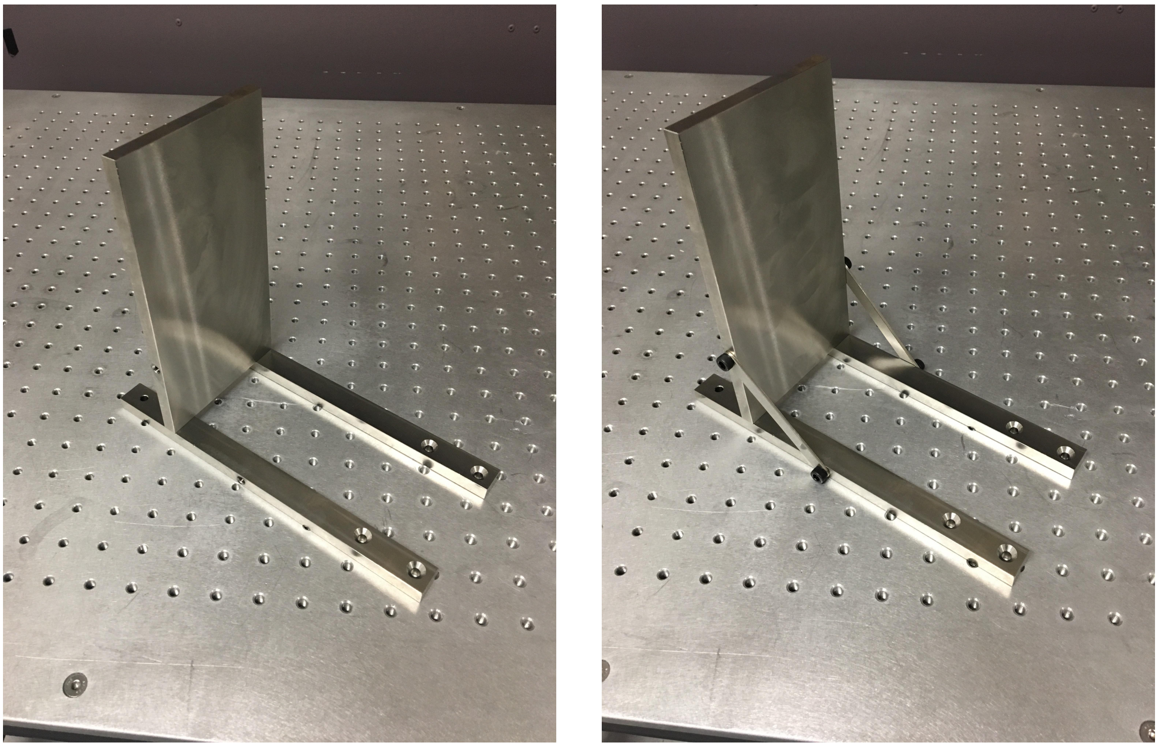

(a) Iteration 2. (b) Iteration 3.

Figure 14: Impinging plate design iterations.

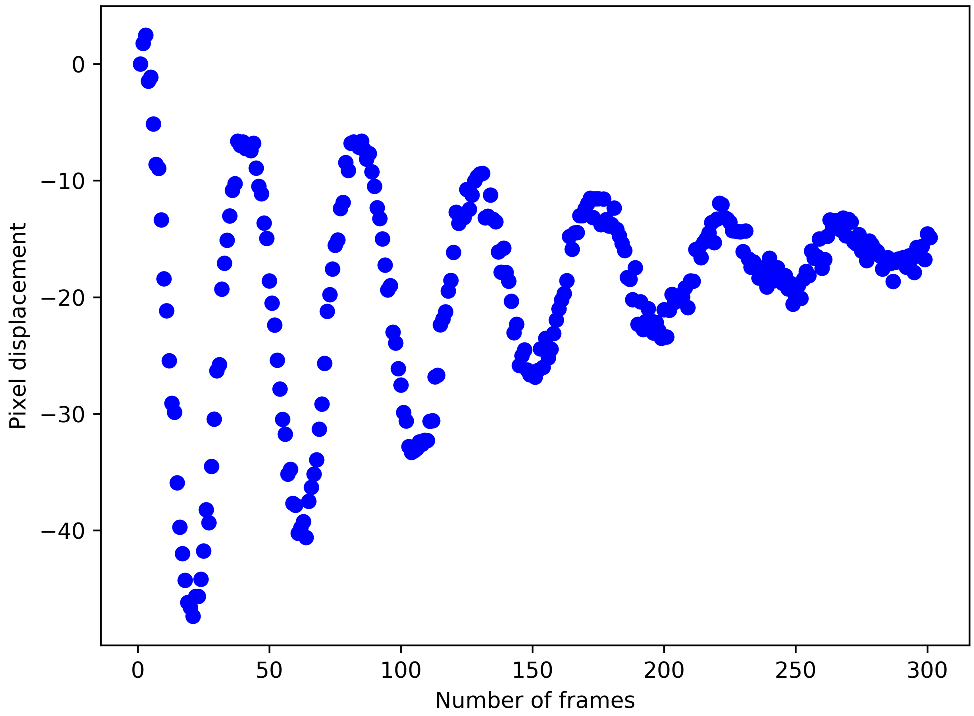

Figure 15: Plate displacement for design iteration 1.

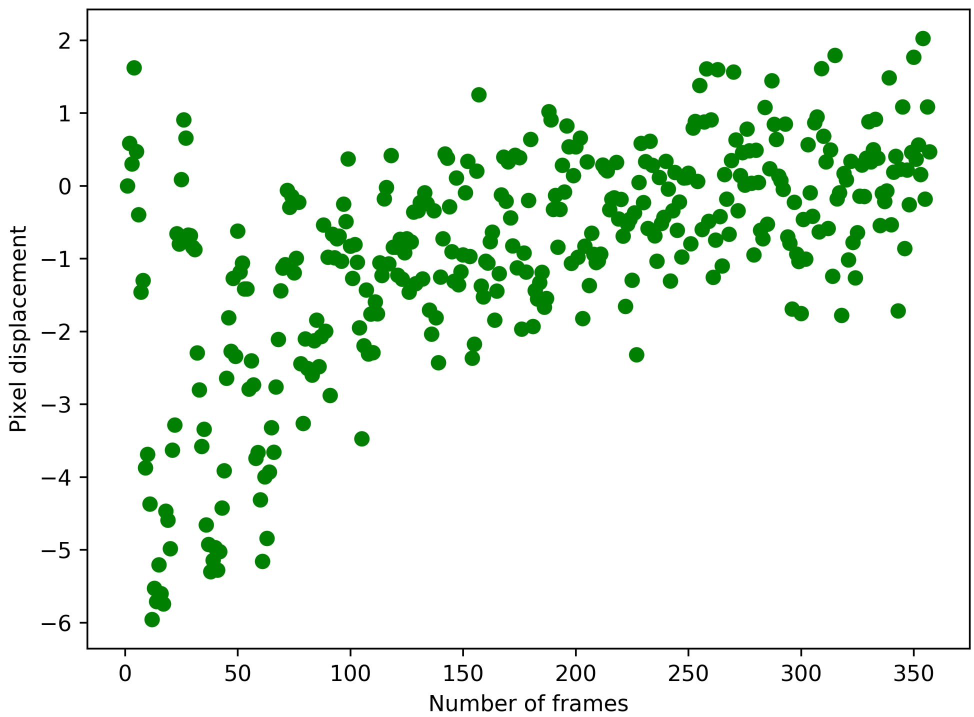

Figure 16: Plate displacement for design iteration 2.

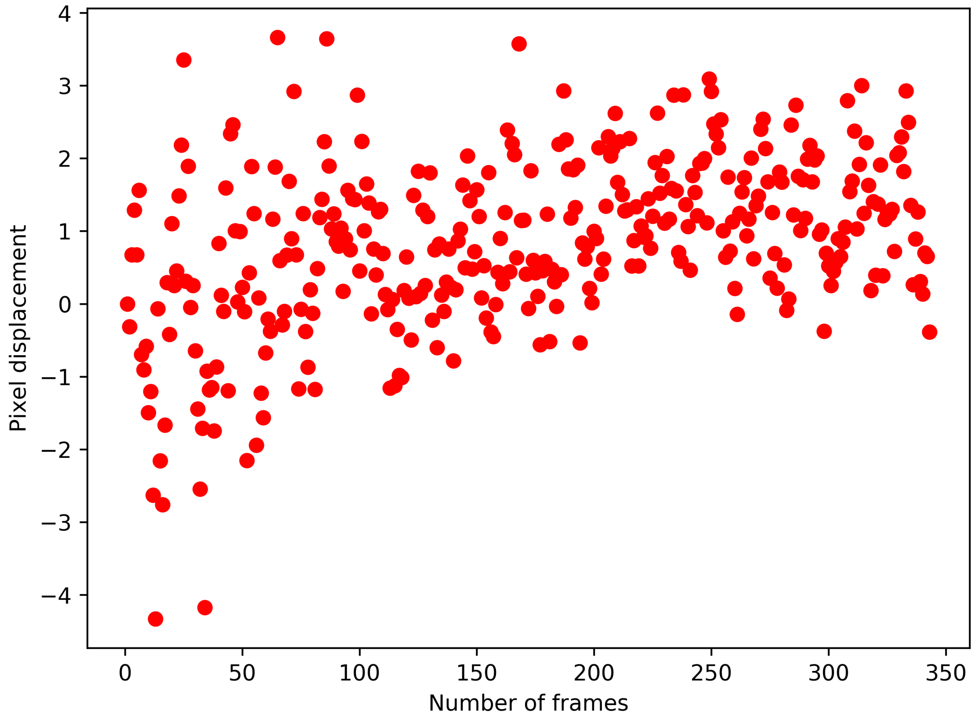

Figure 17: Plate displacement for design iteration 3.

3.4.4 Hydrostatic Test

A hydrostatic test is required of all apparatuses operating under pressurised conditions. The testing of the shock tube driver section involved sealing all non operational valves and pressurising the driver section with water until failure. An air outlet was initially left open and sealed once the driver section was completely filled with water. Figure 20 illustrates the testing configuration used and Table 3 details pressure value limitations and recordings. To comply with manufacturer specifications and design parameters, the high pressure quick release clamp with set to $4Nm$ and the M16 bolts used to construct the driver section were set to $75Nm$. Hydrostatic testing was successfully conducted and resulted in component failure when the driver section pressure exceeded $80bar$. This occurred as a result of an excessive extrusion of the O-ring and is consistent with the high pressure clamp's operational rating. Whilst failure was not the desired outcome, due to the small size of the shock tube's driver section pressurised occurred rapidly and operational limits were exceeded within two pumps of the hydrostatic testing pump. It is believed component failure was the result of stresses exceeding the clamp's material elastic limit. Experimental design operations are not expected to reach similar pressures and as a precaution, the clamp and associated O-ring have been decommissioned. Following a successful hydrostatic test the shock tube driver section was qualified for operation.

Table 3: Hydrostatic test pressure values.

Device	Pressure (Bar)
Clamp rating	82
Driver design	100
Operational maximum	25
Test maximum	>80

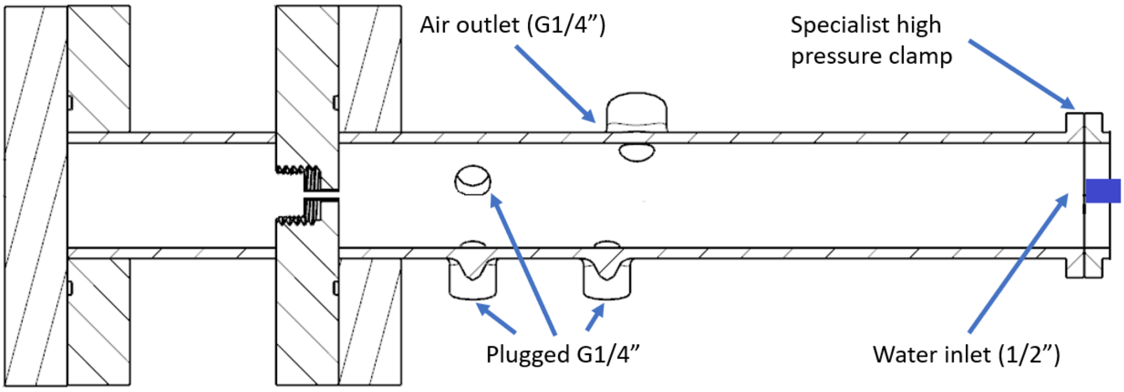

Figure 18: Shock tube drive section hydrostatic test schematic.

3.4.5 Sensor Calibration

Whilst failure was not the desired outcome, due to the small size of the shock tube's driver section pressurised occurred rapidly and operational limits were exceeded within two pumps of the hydrostatic testing pump. It is believed component failure was the result of stresses exceeding the clamp's material elastic limit. Experimental design operations are not expected to reach similar pressures and as a precaution, the clamp and associated O-ring have been decommissioned. Following a successful hydrostatic test the shock tube driver section was qualified for operation.

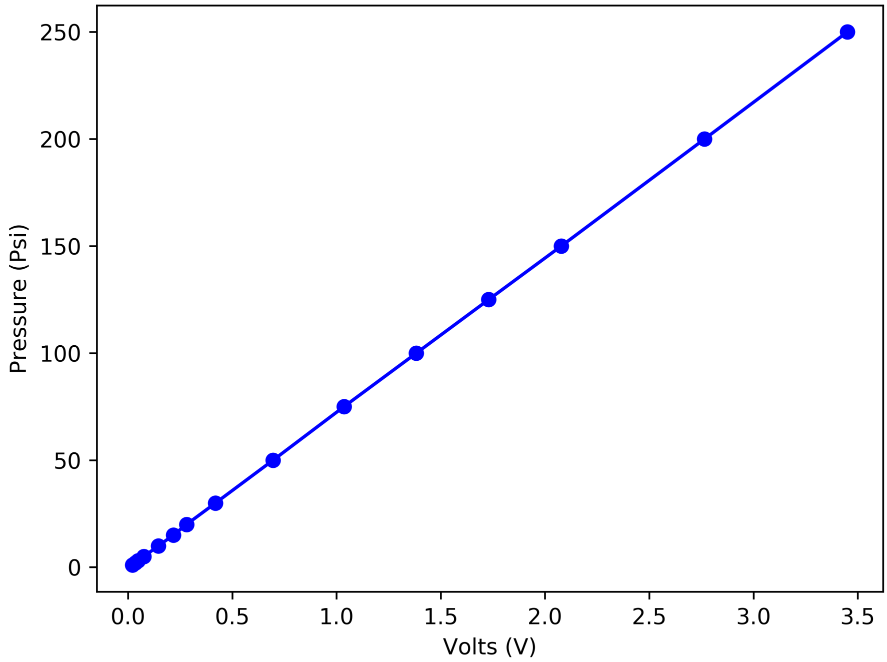

Figure 19: Pressure sensor calibration data(in Psi).

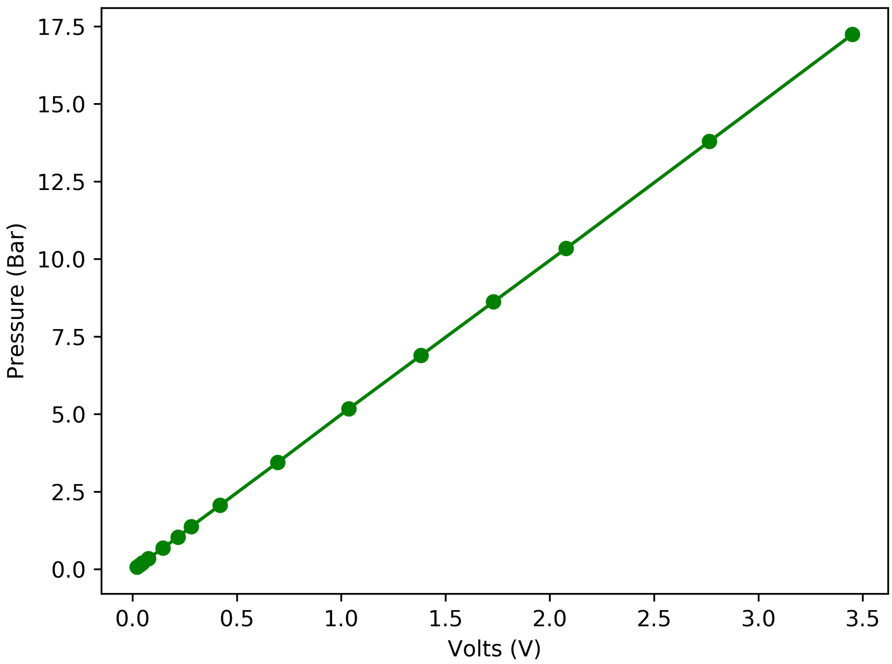

Figure 20: Pressure sensor calibration data(in Bar).

3.4.6 Diaphragm Study

3.4.7 LED Calibration

$$\%_{blur} = \frac{U_i}{T_p * X_{image}} \tag{4}$$

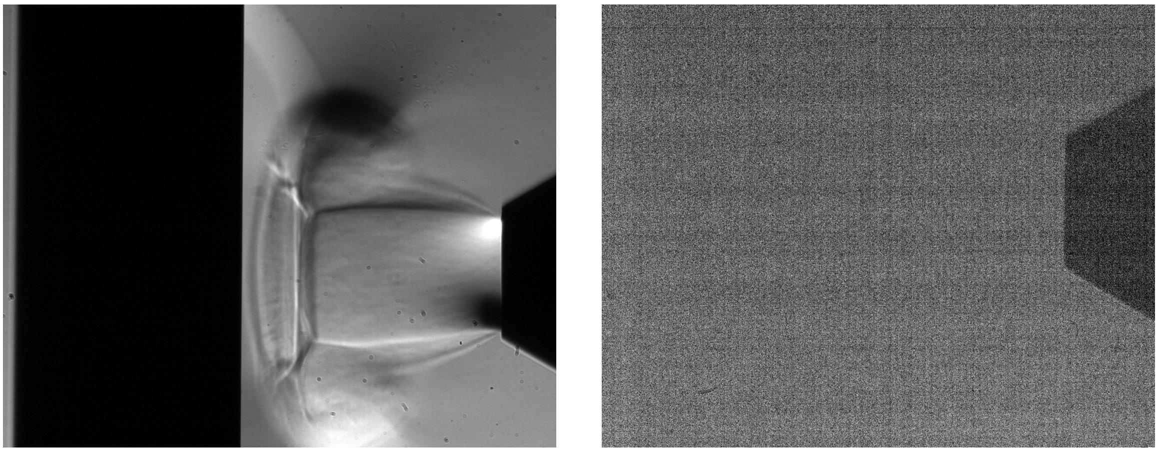

(a) Pulse width = 5ms. (b) Pulse width = 0.5ms.

Figure 21: Pulse width study.

4 Analysis

Schlieren imaging produces a path integrated density gradient image that is excellent for flow visualisation however, it is difficult to quantitatively extract physical parameters directly from image data.

4.1 Second Order Convolution

The first step of the local feature extraction pipeline is to find a set of distinctive keypoints that can be reliably localized under varying imaging conditions, viewpoint changes, and in the presence of noise. In particular, the extraction procedure should yield the same feature locations if the input image is translated or rotated. It is obvious that those criteria cannot be met for all image points. For instance, if we consider a point lying in a uniform region, we cannot determine its exact motion, since we cannot distinguish the point from its neighbors. Similarly, if we consider a point on a straight line, we can only measure its motion perpendicular to the line. This motivates us to focus on a particular subset of points, namely those exhibiting signal changes in two directions. In the following, we will present two keypoint detectors that employ different criteria for finding such regions: the Hessian detector and the H The Hessian detector [Bea78] searches for image locations that exhibit strong derivatives in two orthogonal directions. It is based on the matrix of second derivatives, the so-called Hessian: The detector computes the second derivatives Ixx, Ixy, and Iyy for each image point and then searches for points where the determinant of the Hessian becomes maximal:

The detector computes the second derivatives Ixx, Ixy, and Iyy for each image point and then searches for points where the determinant of the Hessian becomes maximal:

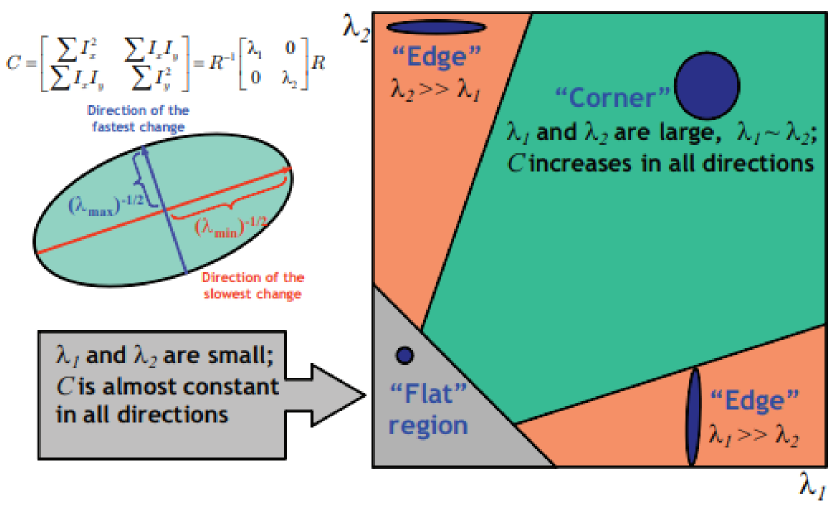

Figure 22: Correspondence between eigenvalues of the Hessian operation and local features (corners, edges, flat regions) [8].

the required second order image derivatives are computed by convolution with the second order derivatives of the Gaussian kernel [29]. Mathematically this means that if f denotes the image and G the normalised Gaussian, we compute EQUATIONS where * denotes spatial convolution, x=(x,y) denotes the pixel position, and the derivative directions i and j can be x or y. The eigenvectors and eigenvalues are computed in the algorithm from a standard second derivative Hessian matrix [30].

HESSIAN MATRIX

Table 4: "Eigenvalues of the Hessian matrix and image structure orientation (L low, H+ high positive, H- high negative)" [1].

λ_1	λ_2	λ_3	Structure orientation
L	L	L	noise (no preferred structure)
L	L	H-	bright sheet-like structure
L	L	H+	dark sheet-like structure
L	H-	H-	bright tubular structure
L	H+	H+	dark tubular structure
H-	H-	H-	bright blob-like structure
H+	H+	H+	dark blob-like structure

4.2 Ranking Methods

Use a normalised ranking to threshold intensity lower then the 90th percentile

5 Results

6 Discussion

7 Conclusions and Recommendations

References

[1] M. Rudzki, "Vessel detection method based on eigenvalues of the hessian matrix and its applicability to airway tree segmentation," in *Proceedings of the 11th International PhD Workshop OWD*, pp. 100–105, 2009.

[2] P. Akbari and R. Nalim, "Review of recent developments in wave rotor combustion technology," *Journal of Propulsion and Power*, vol. 25, no. 4, pp. 833–844, 2009.

[3] B. W. Skews, "The perturbed region behind a diffracting shock wave," *Journal of Fluid Mechanics*, vol. 29, no. 4, pp. 705–719, 1967.

[4] J. J. P. Fernández and J. Sesterhenn, "Compressible starting jet: Pinch-off and vortex ring–trailing jet interaction," *Journal of Fluid Mechanics*, vol. 817, pp. 560–589, 2017.

[5] A. Szumowski, G. Sobieraj, W. Selerowicz, and J. Piechna, "Starting jet–wall interaction," *Journal of sound and vibration*, vol. 232, no. 4, pp. 695–702, 2000.

[6] B. Thethy, "Influence of nozzle geometry on detonation-driven and shock-driven transient supersonic jet flow," *ISABE*, 2019.

[7] G. Settles, "Schlieren and shadowgraph techniques- visualizing phenomena in transparent media(book)," *Berlin, Germany: Springer-Verlag GmbH, 2001.*, 2001.

[8] K. Grauman and B. Leibe, "Visual object recognition," *Synthesis lectures on artificial intelligence and machine learning*, vol. 5, no. 2, pp. 1–181, 2011.

[9] B. Cantwell, "Fundamentals of compressible flow," 2017.

[10] D. Paxson, "Pressure-gain combustion for gas turbines," 2018.

[11] S. Gülen, "Constant volume combustion: The ultimate gas turbine cycle," *Gas Turbine World*, vol. 43, no. 6, pp. 20–27, 2013.

[12] S. Eidelman, W. Grossmann, and I. Lottati, "Review of propulsion applications and numerical simulations of the pulsed detonation engine concept," *Journal of Propulsion and Power*, vol. 7, no. 6, pp. 857–865, 1991.

[13] K. Kailasanath, "Research on pulse detonation combustion systems: a status report," in *47th AIAA aerospace sciences meeting including the new horizons forum and aerospace exposition*, p. 631, 2009.

[14] A. J. Dean, A. Rasheed, V. Tangirala, and P. F. Pinard, "Operation and noise transmission of an axial turbine driven by a pulse detonation combustor," in *ASME Turbo Expo 2005: Power for Land, Sea, and Air*, pp. 1275–1284, American Society of Mechanical Engineers, 2005.

[15] M. I. Radulescu and C. K. Law, "The transient start of supersonic jets," *Journal of Fluid Mechanics*, vol. 578, pp. 331–369, 2007.

[16] R. Ishii, H. Fujimoto, N. Hatta, and Y. Umeda, "Experimental and numerical analysis of circular pulse jets," *Journal of Fluid Mechanics*, vol. 392, pp. 129–153, 1999.

[17] F. Elder Jr and N. De Haas, "Experimental study of the formation of a vortex ring at the open end of a cylindrical shock tube," *Journal of Applied Physics*, vol. 23, no. 10, pp. 1065–1069, 1952.

[18] C. Dora, T. Murugan, S. De, and D. Das, "Role of slipstream instability in formation of counter-rotating vortex rings ahead of a compressible vortex ring," *Journal of Fluid Mechanics*, vol. 753, pp. 29–48, 2014.

[19] T. MATSUDA, Y. UMEDA, R. ISHII, and K. SAWADA, "Numerical and experimental studies on choked underexpanded jets," in *19th AIAA, Fluid Dynamics, Plasma Dynamics, and Lasers Conference*, p. 1378, 1987.

[20] M. Gharib, E. Rambod, and K. Shariff, "A universal time scale for vortex ring formation," *Journal of Fluid Mechanics*, vol. 360, pp. 121–140, 1998.

[21] W. Zhao, S. H. Frankel, and L. G. Mongeau, "Effects of trailing jet instability on vortex ring formation," *Physics of Fluids*, vol. 12, no. 3, pp. 589–596, 2000.

[22] T. Minota, M. Nishida, and M. Lee, "Shock formation by compressible vortex ring impinging on a wall," *Fluid dynamics research*, vol. 21, no. 3, p. 139, 1997.

[23] R. Mariani, K. Kontis, and N. Gongora-Orozco, "Head on collisions of compressible vortex rings on a smooth solid surface," *Shock Waves*, vol. 23, no. 4, pp. 381–398, 2013.

[24] T. Murugan and D. Das, "Characteristics of noise produced during impingement of a compressible vortex ring on a wall," *International Journal of Aeroacoustics*, vol. 9, no. 6, pp. 849–858, 2010.

[25] C. E. Willert, D. M. Mitchell, and J. Soria, "An assessment of high-power light-emitting diodes for high frame rate schlieren imaging," *Experiments in fluids*, vol. 53, no. 2, pp. 413–421, 2012.

[26] J. N. Bradley, *Shock waves in chemistry and physics*. Methuen, 1962.

[27] J. D. Anderson Jr, *Fundamentals of aerodynamics*. Tata McGraw-Hill Education, 2010.

[28] L. Poldervaart, A. Vink, and A. Wijnands, "The photographic evidence of the feedback loop of a two dimensional screeching supersonic jet of air," in *Proceedings of the 6th International Congress on Acoustics, Tokyo, Japan*, 1968.

[29] T. Lindeberg and B. M. ter Haar Romeny, "Linear scale-space i: Basic theory," in *Geometry-driven diffusion in computer vision*, pp. 1–38, Springer, 1994.

[30] E. Meijering, M. Jacob, J.-C. Sarria, P. Steiner, H. Hirling, and M. Unser, "Design and validation of a tool for neurite tracing and analysis in fluorescence microscopy images," *Cytometry Part A: the journal of the International Society for Analytical Cytology*, vol. 58, no. 2, pp. 167–176, 2004.

[31] M. Thangadurai and D. Das, "Experimental study on a compressible vortex ring in collision with a wall," *Journal of visualization*, vol. 15, no. 4, pp. 321–332, 2012.

A Shock Facility

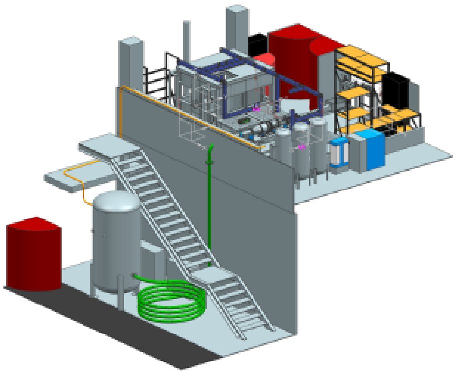

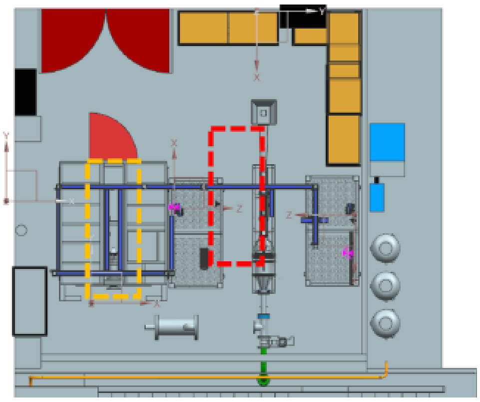

Figure 23: (Left): Isometric view of the LTRAC Shock Lab, with the shock tube facility stored under the shelving. (Right): Top view of the LTRAC Shock Lab, with the PIV (orange) and schlieren (red) sites highlighted.

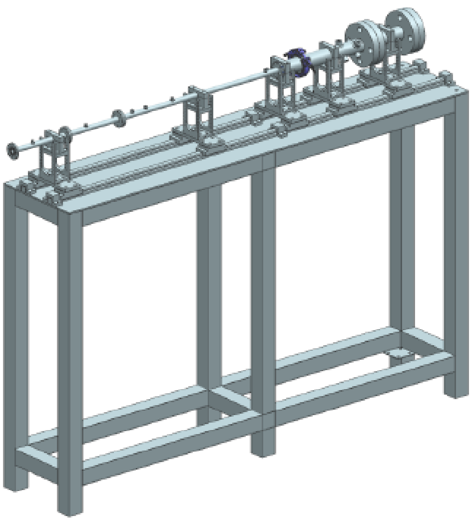

Figure 24: Isometric view of the design of the shock tube facility. (Right): Progress of the commission of the shock tube facility.

B Literature Comparison

Initially, it is necessary to explore the literature and develop an understanding of the current comprehension of the flow characteristics governing supersonic transient jet impingement, and previous experimental test configurations. Section 2 undertakes an extensive review of previous literature, exploring the fluid dynamics and practical applications of supersonic impinging jets. Table 5 details a summary for the research undertaken in previous literature, it's important to note all previous literature sources implement a plate diameter such that it can be considered infinite to the flow. Additionally, imaging results from the literature summarised in Table 1 is subsequently shown in appendix **??**.

Table 5: Literature Summary

Reference	Main Research Focus	Imaging Technique	Inner Shock Tube Diameter	Incident Mach Number	Impingement Plate Distance (inner diameter)
[22]	Shock-vortex interaction in the flow field	Shadowgraph	40mm	1.35	0.4di
[5]	Sound generation upon impingement	Schlieren	65mm	1.14	2di
[24]	Noise due to shock-vortex interaction and impingement	High-speed smoke flow visualisations.	64mm	1.31 - 1.55	4.7di
[31]	Vortex ring impingement	High-speed smoke flow visualisations.	64mm	1.31 - 1.85	4.7di
[23]	Vortex ring impingement	Schlieren	30mm	1.61	1.66di, 3.33di, 5.00di

C Shock Relations

In this section, the relationship between the pressure of the flow behind the leading shock and the ambient pressure will be derived. Figure 25 details pressure, temperature, and velocity relations for the shock tube.

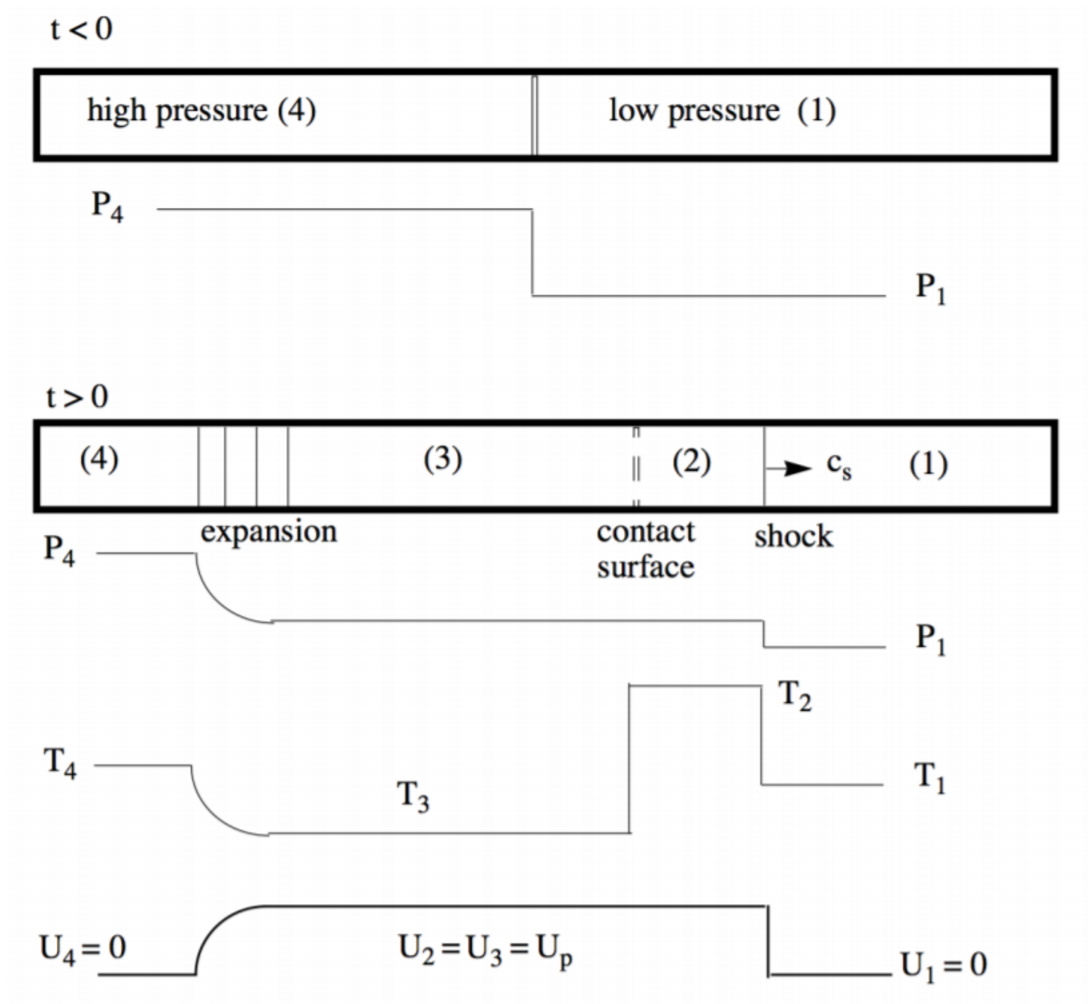

Figure 25: Shock tube flow regions: Region 1 is the flow ahead of the primary shock, region 2 is between contact surface and primary shock, region 3 is between tail of the expansion fan and contact surface, region 4 is ahead of the leading expansion wave [9].

In the following we will combine the results for expansion waves with normal shock relations to derive the so-called shock tube equation. The conditions at the contact surface are:

$$P_2 = P_3 \tag{5}$$

$$U_2 = U_3 = U_p. \tag{6}$$

where U_2 is the speed of the slug of gas set into motion by the opening of the diaphragm.

This is the effective piston speed of the fluid released by the diaphragm.

In a frame of reference moving with the shock wave the gas velocities are

$$U_1' = -c_s \tag{7}$$

$$U_2' = -c_s + U_p \tag{8}$$

and the shock jump conditions are

$$\frac{U_2'}{U_1'} = \frac{1+\frac{\gamma_1-1}{2}M_1^2}{\frac{\gamma_1+1}{2}M_1^2} \tag{9}$$

$$\frac{P_2}{P_1} = \frac{\gamma_1 M_1^2 - \frac{\gamma_1-1}{2}}{\frac{\gamma_1+1}{2}} \tag{10}$$

where $M_1 = c_s/a_1 = -U_1'/a_1$. Using the first relation, Equation 5 above, we can write

$$\frac{U_2'-U_1'}{U_1'} = \frac{1+\frac{\gamma_1-1}{2}M_1^2}{\frac{\gamma_1+1}{2}M_1^2} - 1 = \frac{1-M_1^2}{\frac{\gamma_1+1}{2}M_1^2} \tag{11}$$

The piston velocity is

$$U_p = U_2' - U_1' = U_1'\left(\frac{1-M_1^2}{\frac{\gamma_1+1}{2}M_1\frac{-U_1'}{a_1}}\right) = a_1\left(\frac{M_1^2-1}{\frac{\gamma_1+1}{2}M_1}\right) \tag{12}$$

Note that U_p is positive. Using the second relation, Equation 5, Equation 8 can be expressed in terms of the shock pressure ratio as

$$U_p = a_1\left(\frac{P_2}{P_1}-1\right)\left(\frac{2}{\gamma_1(\gamma_1+1)(P_2/P_1)+\gamma_1(\gamma_1-1)}\right)^{1/2} \tag{13}$$

Equation 9 is the expression for the piston velocity derived using normal shock theory. Now lets work out an expression for the piston velocity using isentropic expansion theory. The velocity behind the expansion is

$$U_3 = U_p = \frac{2a_4}{\gamma_4-1}\left(1-\frac{P_3}{P_4}^{\frac{\gamma_4-1}{2\gamma_4}}\right) \tag{14}$$

Equate 9 and 10.

$$a_1\left(\frac{P_2}{P_1}-1\right)\left(\frac{2}{\gamma_1(\gamma_1+1)(P_2/P_1)+\gamma_1(\gamma_1-1)}\right)^{1/2} = \frac{2a_4}{\gamma_4-1}\left(1-\left(\frac{P_3}{P_2}\frac{P_2}{P_1}\frac{P_1}{P_4}\right)^{\frac{\gamma_4-1}{2\gamma_4}}\right) \tag{15}$$

Using the following identity

$$\frac{P_3}{P_4} = \frac{P_3}{P_2}\frac{P_2}{P_1}\frac{P_1}{P_4} \tag{16}$$

and noting that $P_3/P_2 = 1$ solve Equation 10 for $P_4/P_3 = 1$, substituting in P_2/P_1 from Equation 6. Simplifying, the result is the basic shock tube equation

$$\frac{P_4}{P_1} = \frac{2\gamma_1 M_1^2-(\gamma_1-1)}{\gamma_1+1}\left(1-\frac{\gamma_{4-1}}{\gamma_{1+1}}\frac{U_1}{U_4}\left(M_1-\frac{1}{M_1}\right)\right)^{-2\gamma_4/\gamma_{4-1}} \tag{17}$$

And given the specific gas information, for the driver helium, $\gamma_4 = 1.667$, and the driven air, $\gamma_1 = 1.4$. Taking the ambient air temperature $T_1 = 273.15K$, the relation in Equation 17 can be shown in the Figure 7. This figure highlights the relationship between the driver pressure ratio at 4, and the ambient pressure at 1, for a design incident Mach number. The figure also illustrates the reduced pressure ratio benefit of using a helium to air experiment in comparison to an air to air experiment.